Residual moveout-based wave-equation migration velocity analysis in 3-D

Yang Zhang and Biondo Biondi

ABSTRACT

In the previous report (SEP-143), we proposed a novel approach to perform Wave-Equation Migration Velocity Analysis (WEMVA) using Residual Moveout (RMO) parameters. The 2-D examples we tested showed that this approach is immune to the cycle-skipping problem, and it produces high-quality gradients. In this paper, we try to address the theoretical and practical challenges of extending this method to three-dimensions. Specifically, we propose a new parameterization for the 3-D angle-domain residual moveout and a generalized 3-D RMO-based WEMVA theory. We also address the practical issues in 3-D transforms between subsurface offset and angle-domain image gathers.

INTRODUCTION

Wave-equation migration velocity analysis (WEMVA) (Biondi and Sava, 1999; Biondi and Symes, 2004) belongs to a family of methods for solving the reflection tomography problem. These methods aim to estimate migration velocity by employing wave-equation operators. WEMVA formulates velocity estimation as an optimization problem. Evaluating the flatness of the angle-domain common-image gathers (ADCIGs) is currently the most favored choice when formulating WEMVA objective functions. The WEMVA objective function is optimized by applying gradient-based algorithms. The computation of the gradient is performed in two steps:

1. Computation of a perturbation in the migrated image.
2. Back-projection of the image perturbation into the velocity model using the image-domain wave-equation tomographic operator.

In the previous report (Zhang and Biondi, 2011), we proposed a new WEMVA method for maximizing the angle-stack power of ADCIGs. The key innovations in this method are as follows: first, we approximate the ADCIG, $I(s)$ (migrated using the current slowness s), with the initial ADCIG $I(s_0)$ followed by an RMO(Residual Moveout) on $I(s_0)$; then we design a new image-space tomography operator that describes the kinematic relation between the model slowness perturbation and the RMO parameters. Using several 2-D examples, we have shown that this method: 1) avoids cycle-skipping, 2) does not require manual picking of the moveout parameters, and 3) can robustly improve the flatness of the angle gathers.

Although the three-dimensional extension of our method is conceptually straightforward, to actually implement a 3-D prototype requires substantial efforts on both the theoretical and practical aspects. In this paper, we present our initial work toward a 3-D implementation of our approach. The rest of the paper is organized as follows: First, we present the upgraded theory of our RMO WEMVA method for handling 3-D ADCIGs. Second, we discuss some of the challenges of transforming 3D common-image gathers (CIGs) between the offset and angle domains. We show a synthetic example as a prove of concept for our 3-D RMO WEMVA formulation.

3-D RMO WEMVA METHOD

We first review the rationale and key derivations of our RMO WEMVA theory in the 2-D case, and then present the 3-D generalization to the theory by making analogies. Practical experience indicates that slowness is a better parameterization than velocity. For clarity, the model space is parameterized as slowness unless otherwise specified.

2-D Theory Review

We start from the 'classical' maximum-stack-power objective function

$$J(s) = \frac{1}{2}\sum_x\sum_z\left[\sum_\gamma I(z,\gamma,x;s)\right]^2, \tag{1}$$

where s is the model slowness, and $I(z,\gamma,x;s)$ is the prestack image (ADCIGs) migrated with s.

Objective functions defined this way are prone to cycle-skipping (Symes, 2008). To tackle this issue, we *approximate* objective function 1 with the following one:

$$J(\rho(s)) = \frac{1}{2}\sum_x\sum_z\left[\sum_\gamma I(z+\rho\tan^2\gamma,\gamma,x;s_0)\right]^2, \tag{2}$$

in which s is the model slowness, $I(z,\gamma,x;s_0)$ is the prestack image migrated with some initial slowness s_0, and $\rho\tan^2\gamma$ is the residual moveout (RMO) function we choose to characterize the kinematic difference (Biondi and Symes, 2004) between $I(s)$ and $I(s_0)$.

The meaning of equation 2 can be easily explained. As the model changes from s_0 to s, it leads to the change of the image kinematics between $I(s_0)$ and $I(s)$, where the differences are characterized by the moveout parameter ρ. Since $I(s)$ will be *kinematically the same* as $I(s_0)$ being applied moveout $\rho(s)$, if we substitute the former image ($I(s)$) with the latter one, we transit from equation 1 to equation 2. *Notice that the new objective function is expressed as a function of only the moveout parameter ρ, while the ρ parameter is then related to the model slowness s.*

Furthermore, notice that equation 2 weights the strong-amplitude events more heavily. To make the gradient independent from the strength of reflectors, we further replace 2 with the following semblance objective function:

$$J_{Sm}(\rho(s)) = \frac{1}{2}\sum_x \sum_z \frac{\sum_{z_w}\left(\sum_\gamma I(z + z_w + \rho\tan^2\gamma, \gamma, x; s_0)\right)^2}{\sum_{z_w}\sum_\gamma I^2(z + z_w + \rho\tan^2\gamma, \gamma, x; s_0)}, \tag{3}$$

where z_w is a local averaging window of length L along the depth axis. For the rest of the paper, the summation interval of z_w is always $[-L/2, L/2]$; thus we can safely omit the summation bounds for concise notation.

We will use gradient-based methods to solve this optimization problem. The gradient given by the objective function 3 is

$$\frac{\partial J_{S_m}}{\partial s} = \frac{\partial J_{S_m}}{\partial \rho}\frac{\partial \rho}{\partial s}, \tag{4}$$

where $\partial J_{S_m}/\partial \rho$ can be easily calculated by taking the derivative along the ρ axis of the semblance panel S_m.

To evaluate the derivative of the moveout parameter ρ with respect to the slowness model s, we define an auxiliary objective function in a fashion similar to the one employed by Luo and Schuster (1991) for cross-well travel-time tomography. The auxiliary objective function is defined for each image point (z, x) as:

$$J_{\text{aux}} = \sum_{z_w}\sum_\gamma I(z + z_w + (\rho\tan^2\gamma + \beta), \gamma, x; s_0) I(z, \gamma, x; s) \tag{5}$$

where β is a simple vertical shift introduced to accommodate bulk shifts in the image introduced by variation in the migration velocity. Notice that the semblance in objective function 3 is independent of β because a bulk shift does not affect the power of the stack; therefore we do not include β in 3.

The explanation for equation 5 is as follows: The moveout parameters $\beta(s)$ and $\rho(s)$ are chosen to describe the kinematic difference between the initial image $I(z, \gamma, x; s_0)$ and the new image $I(z, \gamma, x; s)$. In other words, if we apply the moveout to the initial image, the resulting image $I(z + (\rho\tan^2\gamma + \beta), \gamma, x; s_0)$ will be the same as the new image $I(z, \gamma, x; s)$ in terms of kinematics; this is indicated by a maximum of the cross-correlation between the two.

Given the auxiliary objective function 5, $\partial\rho/\partial s$ can be found using the rule of partial derivatives for implicit functions. We compute the gradient of 5 around the maximum at $s = s_0$ and $\rho = \beta = 0$; consequently

$$\begin{cases} \frac{\partial J_{\text{aux}}}{\partial \rho} = 0 \\ \frac{\partial J_{\text{aux}}}{\partial \beta} = 0 \end{cases} \tag{6}$$

We differentiate equation 6 with respect to s, which gives

$$\begin{bmatrix} \frac{\partial^2 J_{\text{aux}}}{\partial\rho^2} & \frac{\partial^2 J_{\text{aux}}}{\partial\rho\partial\beta} \\ \frac{\partial^2 J_{\text{aux}}}{\partial\rho\partial\beta} & \frac{\partial^2 J_{\text{aux}}}{\partial\beta^2} \end{bmatrix} \begin{bmatrix} \frac{\partial\rho}{\partial s} \\ \frac{\partial\beta}{\partial s} \end{bmatrix} = -\begin{bmatrix} \frac{\partial J_{\text{aux}}}{\partial\rho\partial s} \\ \frac{\partial J_{\text{aux}}}{\partial\beta\partial s} \end{bmatrix}. \tag{7}$$

Now we need to invert a Jacobian to get $\partial\rho/\partial s$. We denote $\dot{I}, \ddot{I}$ to be the first and second order z derivatives of image I, then define the following:

$$\begin{aligned} \frac{\partial^2 J_{\text{aux}}}{\partial\rho^2} &= \sum_{z_w}\sum_{\gamma} \ddot{I}(z+z_w,\gamma,x;s_0)\tan^4\gamma I(z+z_w,\gamma,x;s) = E_{11}(z,x) \\ \frac{\partial^2 J_{\text{aux}}}{\partial\rho\partial\beta} &= \sum_{z_w}\sum_{\gamma} \ddot{I}(z+z_w,\gamma,x;s_0)\tan^2\gamma I(z+z_w,\gamma,x;s) = E_{12}(z,x) \\ \frac{\partial^2 J_{\text{aux}}}{\partial\beta^2} &= \sum_{z_w}\sum_{\gamma} \ddot{I}(z+z_w,\gamma,x;s_0) I(z+z_w,\gamma,x;s) = E_{22}(z,x). \end{aligned} \tag{8}$$

Let the inverse of matrix E be matrix F:

$$F = \begin{bmatrix} F_{11} & F_{12} \\ F_{12} & F_{22} \end{bmatrix} = \begin{bmatrix} E_{11} & E_{12} \\ E_{12} & E_{22} \end{bmatrix}^{-1}$$

Then

$$\frac{\partial\rho}{\partial s}|_{s=s_0} = -\sum_{z_w}\sum_{\gamma}(F_{11}\tan^2\gamma + F_{12})\dot{I}(z+z_w,\gamma,x;s_0)\frac{\partial I(z+z_w,\gamma,x;s)}{\partial s}. \tag{9}$$

Finally, we have the expression for the gradient

$$-\sum_{z_w}\sum_{\gamma}\sum_{z,x}\frac{\partial I(z+z_w,\gamma,x;s)}{\partial s}(F_{11}\tan^2\gamma + F_{12})\frac{\partial J_{Sm}}{\partial\rho}(z,x)\dot{I}(z+z_w,\gamma,x;s_0). \tag{10}$$

The engineering translation of equation 10 is that first we compute the image perturbation $(F_{11}\tan^2\gamma + F_{12})\frac{\partial J_{Sm}}{\partial\rho}(z,x)\dot{I}(z+z_w,\gamma,x;s_0)$, then we backproject this perturbation to model slowness space using the tomography operator $\partial I(z+z_w,\gamma,x;s)/\partial s$.

Since we can compute the gradient in equation 10, any gradient-based optimization method can be used to maximize the objective function defined in equation 3. Nonetheless, in terms of finding the step size, it is more expensive to evaluate equation 3 (which is an approximation of equation 1 purely based on kinematics) than to evaluate the original objective function 1. In our implementation we choose 1 as the maximization goal while using the search direction computed from equation 3.

Extension to 3-D

As we shift from 2-D seismic surveys to 3-D ones, two extra dimensions (cross-line axis y and subsurface azimuth ϕ) are added to our seismic image. Therefore we denote the prestack image as $I(z, \gamma, \phi, x, y)$. Assuming there are m values for ϕ, then $\phi \in \{\phi_i : i = 1, 2, ..., m\}$. Now the maximum-stack-power objective function 1 can be generalized to

$$J(s) = \frac{1}{2} \sum_{x,y} \sum_{z} \left[\sum_{\phi_i} \sum_{\gamma} I(z, \gamma, \phi_i, x, y; s) \right]^2, \tag{11}$$

in which we stack the gather along both γ and ϕ axes.

The next step is to choose a proper residual moveout parameterization for the 3-D ADCIGs, in which the moveout is a surface (defined by (γ, ϕ)) rather than a curve (of γ). There are certainly more than one way to design such parameterization. As an initial attempt, we choose a straightforward approach, in which we separate the moveout surface into individual curves by azimuth ϕ. For each azimuth angle ϕ_i, we assign the curvature parameter ρ_i and the static shift parameter β, respectively. *Notice that all the curves share the same* β *parameter, because the center of the moveout surface at* $(\gamma = 0, \forall \phi_i)$ *is shared by all curves.*

Under this parameterization, the 3-D counterpart of objective function 3 would be

$$J_{Sm}(\rho(s)) = \frac{1}{2} \sum_{x,y} \sum_{z} \sum_{\phi_i} \frac{\sum_{z_w} \left(\sum_{\gamma} I(z + z_w + \rho_i \tan^2 \gamma, \gamma, \phi_i, x, y; s_0) \right)^2}{\sum_{z_w} \sum_{\gamma} I^2(z + z_w + \rho_i \tan^2 \gamma, \gamma, \phi_i, x, y, ; s_0)}, \tag{12}$$

where ρ *becomes a vector*, $\rho = \{\rho_i : i = 1, 2, ..., m\}$. The gradient formula 4 now turns into

$$\frac{\partial J_{S_m}}{\partial s} = \sum_{\rho_i} \frac{\partial J_{S_m}}{\partial \rho_i} \frac{\partial \rho_i}{\partial s}. \tag{13}$$

Because each ϕ_i is treated separately, we can compute $\partial J_{Sm} / \partial \rho_i$ in exactly the same way as we do in the 2-D case.

Analogously, we can define an auxiliary objective function for each image point that uncovers the $s \leftrightarrow \rho$ relationship:

$$J_{\text{aux}} = \sum_{z_w} \sum_{\gamma} \sum_{\phi_i} I(z + z_w + (\rho_i \tan^2 \gamma + \beta), \gamma, \phi_i, x, y; s_0) I(z, \gamma, \phi_i, x, y; s). \tag{14}$$

Using the same trick of finding partial derivatives for implicit functions, equation 6 is generalized as

$$\begin{cases} \frac{\partial J_{\text{aux}}}{\partial \rho_1} = 0 \\ \frac{\partial J_{\text{aux}}}{\partial \rho_2} = 0 \\ \quad \vdots \\ \frac{\partial J_{\text{aux}}}{\partial \rho_m} = 0 \\ \frac{\partial J_{\text{aux}}}{\partial \beta} = 0 \end{cases} \tag{15}$$

We differentiate equation 15 with respect to s:

$$\begin{bmatrix} \frac{\partial^2 J_{\text{aux}}}{\partial {\rho_1}^2} & \frac{\partial^2 J_{\text{aux}}}{\partial \rho_1 \partial \rho_2} & \cdots & \frac{\partial^2 J_{\text{aux}}}{\partial \rho_1 \partial \rho_m} & \frac{\partial^2 J_{\text{aux}}}{\partial \rho_1 \partial \beta} \\ \frac{\partial^2 J_{\text{aux}}}{\partial \rho_2 \partial \rho_1} & \frac{\partial^2 J_{\text{aux}}}{\partial {\rho_2}^2} & \cdots & \frac{\partial^2 J_{\text{aux}}}{\partial \rho_2 \partial \rho_m} & \frac{\partial^2 J_{\text{aux}}}{\partial \rho_2 \partial \beta} \\ \vdots & \vdots & \vdots & \vdots & \vdots \\ \frac{\partial^2 J_{\text{aux}}}{\partial \rho_m \partial \rho_1} & \frac{\partial^2 J_{\text{aux}}}{\partial \rho_m \partial \rho_2} & \cdots & \frac{\partial^2 J_{\text{aux}}}{\partial {\rho_m}^2} & \frac{\partial^2 J_{\text{aux}}}{\partial \rho_m \partial \beta} \\ \frac{\partial^2 J_{\text{aux}}}{\partial \beta \partial \rho_1} & \frac{\partial^2 J_{\text{aux}}}{\partial \beta \partial \rho_2} & \cdots & \frac{\partial^2 J_{\text{aux}}}{\partial \beta \partial \rho_m} & \frac{\partial^2 J_{\text{aux}}}{\partial \beta^2} \end{bmatrix} \begin{bmatrix} \frac{\partial \rho_1}{\partial s} \\ \frac{\partial \rho_2}{\partial s} \\ \vdots \\ \frac{\partial \rho_m}{\partial s} \\ \frac{\partial \beta}{\partial s} \end{bmatrix} = - \begin{bmatrix} \frac{\partial^2 J_{\text{aux}}}{\partial \rho_1 \partial s} \\ \frac{\partial^2 J_{\text{aux}}}{\partial \rho_2 \partial s} \\ \vdots \\ \frac{\partial^2 J_{\text{aux}}}{\partial \rho_m \partial s} \\ \frac{\partial^2 J_{\text{aux}}}{\partial \beta \partial s} \end{bmatrix}. \tag{16}$$

We can calculate the $m+1$ by $m+1$ Jacobian matrix elements and the right-hand side based on equation 14:

$$\begin{aligned} \frac{\partial^2 J_{\text{aux}}}{\partial {\rho_i}^2} &= \sum_{z_w} \sum_{\gamma} \ddot{I}(z+z_w,\gamma,\phi_i,x,y;s_0) \tan^4 \gamma I(z+z_w,\gamma,\phi_i,x,y;s) \\ \frac{\partial^2 J_{\text{aux}}}{\partial \rho_i \partial \rho_j} &\equiv 0 \qquad\qquad \forall \quad i \neq j \\ \frac{\partial^2 J_{\text{aux}}}{\partial \rho_i \partial \beta} &= \sum_{z_w} \sum_{\gamma} \ddot{I}(z+z_w,\gamma,\phi_i,x,y;s_0) \tan^2 \gamma I(z+z_w,\gamma,\phi_i,x,y;s) \\ \frac{\partial^2 J_{\text{aux}}}{\partial \beta^2} &= \sum_{z_w} \sum_{\gamma} \sum_{\phi_i} \ddot{I}(z+z_w,\gamma,\phi_i,x,y;s_0) I(z+z_w,\gamma,\phi_i,x,y;s) \\ \frac{\partial^2 J_{\text{aux}}}{\partial \rho_i \partial s} &= \sum_{z_w} \sum_{\gamma} \dot{I}(z+z_w,\gamma,\phi_i,x,y;s_0) \tan^2 \gamma \frac{\partial I(z+z_w,\gamma,\phi_i,x,y;s)}{\partial s} \\ \frac{\partial^2 J_{\text{aux}}}{\partial \beta \partial s} &= \sum_{z_w} \sum_{\gamma} \sum_{\phi_i} \dot{I}(z+z_w,\gamma,\phi_i,x,y;s_0) \frac{\partial I(z+z_w,\gamma,\phi_i,x,y;s)}{\partial s}. \end{aligned} \tag{17}$$

Denoting matrix $\mathbf{F} = \{F_{i,j}\}$ to be the inverse of the Jacobian, then

$$\begin{bmatrix} \frac{\partial \rho_1}{\partial s} \\ \frac{\partial \rho_2}{\partial s} \\ \vdots \\ \frac{\partial \rho_m}{\partial s} \end{bmatrix} = - \begin{bmatrix} F_{1,1} & F_{1,2} & \cdots & F_{1,m-1} & F_{1,m} & F_{1,m+1} \\ F_{2,1} & F_{2,2} & \cdots & F_{2,m-1} & F_{2,m} & F_{2,m+1} \\ \vdots & \vdots & \vdots & \vdots & \vdots & \vdots \\ F_{m-1,1} & F_{m-1,2} & \cdots & F_{m-1,m-1} & F_{m-1,m} & F_{m-1,m+1} \\ F_{m,1} & F_{m,2} & \cdots & F_{m,m-1} & F_{m,m} & F_{m,m+1} \end{bmatrix} \begin{bmatrix} \frac{\partial^2 J_{\text{aux}}}{\partial \rho_1 \partial s} \\ \frac{\partial^2 J_{\text{aux}}}{\partial \rho_2 \partial s} \\ \vdots \\ \frac{\partial^2 J_{\text{aux}}}{\partial \rho_{m-1} \partial s} \\ \frac{\partial^2 J_{\text{aux}}}{\partial \rho_m \partial s} \\ \frac{\partial^2 J_{\text{aux}}}{\partial \beta \partial s} \end{bmatrix}. \tag{18}$$

Finally, plugging equation 18 and 17 back into the model gradient expression 13, we get

$$\frac{\partial J}{\partial s} = - \sum_{z_w} \sum_{\gamma} \sum_{\phi_i} \frac{\partial I(z+z_w,\gamma,\phi_i,x,y;s)}{\partial s} (G_i \tan^2 \gamma + G_{m+1}) \dot{I}(z+z_w,\gamma,\phi_i,x,y;s_0), \tag{19}$$

in which

$$\begin{bmatrix} G_1 & G_2 & \cdots & G_m & G_{m+1} \end{bmatrix} = \begin{bmatrix} \frac{\partial J_{\mathrm{Sm}}}{\partial \rho_1} & \frac{\partial J_{\mathrm{Sm}}}{\partial \rho_2} & \cdots & \frac{\partial \mathrm{J}_{\mathrm{Sm}}}{\partial \rho_m} \end{bmatrix} \begin{bmatrix} F_{1,1} & F_{1,2} & \cdots & F_{1,m} & F_{1,m+1} \\ F_{2,1} & F_{2,2} & \cdots & F_{2,m} & F_{2,m+1} \\ \vdots & \vdots & \vdots & \vdots & \vdots \\ F_{m,1} & F_{m,2} & \cdots & F_{m,m} & F_{m,m+1} \end{bmatrix}. \tag{20}$$

In practice, there are some caveats when taking the inverse of the Jacobian matrix. The Jacobian can be ill-conditioned when all elements in one row or column are close to zero. For example, if the image point is not illuminated from a certain azimuth direction ϕ_j, i.e. $I(z, \gamma, \phi_j, x, y) = 0$, then the j_{th} row and column of the Jacobian would be zero. In order to avoid numerical overflow under this circumstance, we pre-exclude those azimuth angles with poor illumination energy from the Jacobian, and we invert a subset of the original Jacobian that contains only image gathers at well-illuminated azimuth angles.

Gaussian anomaly example

In this example, the model is 2.4 km in x, 2.4 km in y and 1.0 km in z; the grid sampling is 20 m in x and y, 10 m in z. The receivers are fixed during the entire survey, spanning a rectangular area from (−0.8 km, −0.8 km) to (+0.8 km, +0.8 km with receiver spacing of 20 m in both x and y. The shot locations cover the same region as the receivers do, and the shot spacing is 100 m. This leads to a survey of 81 receivers and 17 shots along both x and y. A total of 32 frequencies are calculated, ranging from 5 Hz to 40 Hz. There is one flat reflector at a depth of 0.6 km. A constant starting velocity of 2 km/s is used. The true model is a constant background velocity (2 km/s, same as the starting velocity), but with a 0.6 km width, 0.25 km height Gaussian anomaly at the center, with a peak value of 3 km/s. Figure 1 shows the true velocity model.

First, we compute the initial subsurface ODCIG (offset-domain common-image gather) with the offset hx, hy range being ±100 m. The acquisition geometry we use can provide full azimuth for the inner portion of the model. We choose to generate ADCIGs along three azimuth angles: $0°, 30°$ and $60°$.

Figure 2 shows the derivatives of the semblance objective function over the moveout parameter ρ_i, with each panel representing a distinct azimuth: $0, 30$ and 60 degrees. Since the migration velocity is slower than the true one, most of the ADCIGs would be curving upward, therefore a proper objective function should instruct the inversion to decrease the curvature. Figure 2 verifies the consistency between the numerical result and our theoretical expectation. Notice in each plot, there are some positive values on the direction perpendicular to the azimuth orientation. This is caused by the fact that at these locations, the seismic energy traveling through the designated azimuth probes a much smaller anomaly. (Imagine we have a spheric anomaly centered around the origin: $x^2 + y^2 + z^2 = 1$, the strength of the anomaly decreases by distance from the center. If we intercept the anomaly with vertical plane $y = 0$, the anomaly seen on the section is strong because the section passes through the center of the sphere. However, if we intercept the sphere with $y = 0.7$, the anomaly seen on that plane would be much weaker and smaller, because the part of the anomaly seen on this plane is far away from the center.) In this case, the ADCIG at near angles are affected by the anomaly but the far angles are not, therefore showing the opposite curvature. This phenomenon might hinder the tomography algorithm from finding a good update. Fortunately, with more than one azimuth, the curvatures observed from the alternative azimuth would offset this effect. This example shows one of the advantages of having multiple azimuth image gathers.

Figure 3 shows the first model gradient (in velocity) calculated using our approach. Qualitatively, the method works as we expected. The update is concentrated around the anomaly's location and the sign of the update is correct.

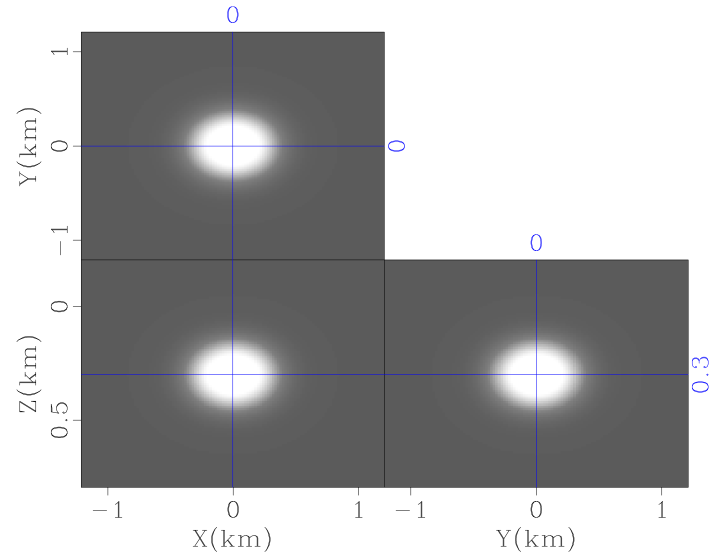

Figure 1: The true velocity model, with positive Gaussian anomaly in the center. [**ER**]

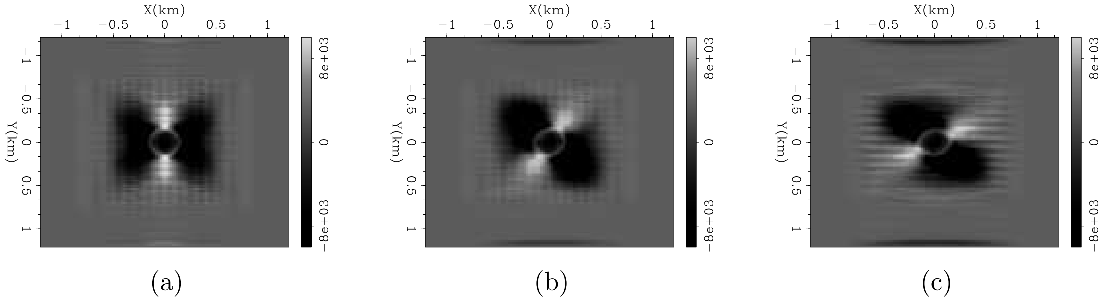

(a) (b) (c)

Figure 2: The $\partial J/\partial \rho_i$ term for (a) $\phi = 0°$, (b) $\phi = 30°$ and (c) $\phi = 60°$. The values correlates well with the curvatures of the ADCIGs at each (x, y) location. [**CR**]

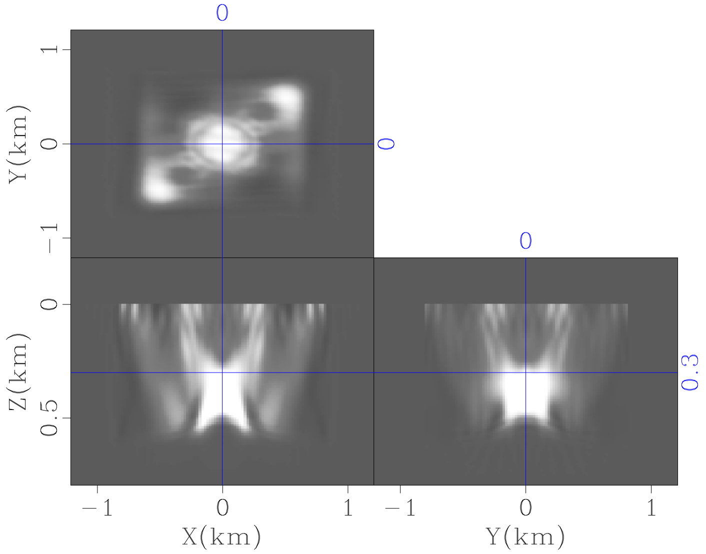

Figure 3: First gradient of the velocity model calculated by our 3-D RMO WEMVA implementation, i.e. Δv predicted by our WEMVA objective function. [**CR**]

3-D transforms between offset and angle domain

Our RMO-based WEMVA approach operate exclusively on subsurface *angle* domain CIGs, however, compared to ADCIGs, subsurface *offset* domain CIGs are much friendlier for computer implementation. The image-space tomographic operator on ODCIGs also has a simpler formula and can be straightforwardly implemented (Tang et al., 2008). Therefore transforming between ODCIGs and ADCIGs is required for our approach. Tisserant and Biondi (2003) and Biondi and Tisserant (2004) presented the theory for this tranformation. We review the key steps in the offset to angle transformation:

1. Perform Fourier transform $I(hx, hy, x, y, z) \rightarrow I(hx, hy, k_x, k_y, k_z)$.
2. For each (k_x, k_y, k_z),
   - apply Fourier transform $I(hx, hy) \rightarrow I(k_{hx}, k_{hy})$
   - map $I(k_{hx}, k_{hy}) \rightarrow I(\gamma, \phi)$ based on the following relations (Tisserant and

Biondi, 2003):

$$\begin{bmatrix} k'_x \\ k'_y \end{bmatrix} = \begin{bmatrix} \cos\phi & -\sin\phi \\ \sin\phi & \cos\phi \end{bmatrix} \begin{bmatrix} k_x \\ k_y \end{bmatrix}$$

$$k'_{hx} = k_z \sqrt{1 + (k'_y/k_z)^2} \tan\gamma$$

$$k'_{hy} = \frac{k'_y k'_x k'_{hx}}{k'^2_y + k^2_z}$$

$$\begin{bmatrix} k_{hy} \\ k_{hy} \end{bmatrix} = \begin{bmatrix} \cos\phi & \sin\phi \\ -\sin\phi & \cos\phi \end{bmatrix} \begin{bmatrix} k'_{hx} \\ k'_{hy} \end{bmatrix}. \tag{21}$$

3. Apply inverse Fourier transform $I(\gamma, \phi, k_x, k_y, k_z) \rightarrow I(\gamma, \phi, x, y, z)$.

Similarly, the backward transform (angle to offset) is done by reversing the order of the procedures above.

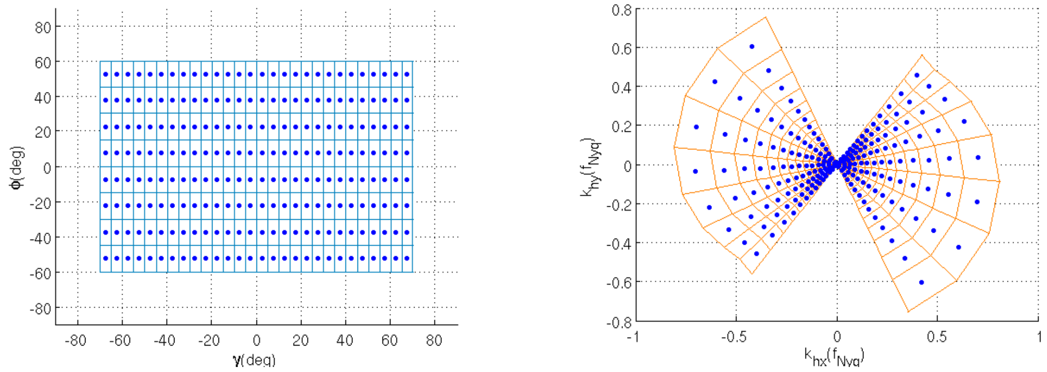

(a) (b)

Figure 4: Graphical illustration of the mapping from the (γ, ϕ) plane to the (k_{hx}, k_{hy}) plane. Each dot in (a) maps to a corresponding dot in (b); similarly, each quadrilateral patch in (a) maps to a corresponding patch in (b). [**CR**]

The mapping between (γ, ϕ) and (k_{hx}, k_{hy}) is highly irregular (Biondi, 2003). Figure 4 shows the mapping from a regularly sampled (γ, ϕ) mesh to the (k_{hx}, k_{hy}) domain given fixed $k_z = 1/2$, $k_x = 1/4$ and $k_y = 1/4$ (assume the Nyquist wave number is 1). We can see the mapping brings distortion, and the density of the samples on (k_{hx}, k_{hy}) becomes non-uniform. A proper interpolation scheme is very important to reduce the artifacts caused by such irregularity. This issue becomes more serious for the backward transform (angle to offset), because the azimuth angle ϕ is usually not sufficiently sampled; simply placing all available samples on the (γ, ϕ) plane onto their mapped locations on (k_{hx}, k_{hy}) plane would leave many holes unfilled. On the other hand, under mapping relation 21, it is easy to map from a given (γ, ϕ) value to (k_{hx}, k_{hy}), but it is difficult to do the reverse due to the algebra. Therefore, it is very difficult to iterate over all points on (k_{hx}, k_{hy}), find the corresponding (γ, ϕ) coordinates, and fetch the values on these coordinates.

We choose a simple yet effective scheme to perform this mapping. Instead of mapping from sample points to sample points (dots in Figure 4), we map from quadrilateral patches to quadrilateral patches, assuming each patch contains uniformly the value of the sample located in its center. We use a classic polygon-filling algorithm for this mapping. After that, a slight amount of smoothing is applied on the output to remove potential discontinuities along the boundaries of the patches.

We use the previous synthetic example to demonstrate the necessity of this scheme. We start with an initial subsurface ODCIG by migrating the data using the starting velocity model, as shown in Figure 5(c). Then we apply our forward and backward offset-angle transforms to the ODCIG sequentially (Figure 5(b)). For comparison, we also compute the result using the transform that simply does sample-to-sample mapping (Figure 5(a)). A good transform pair should make the resulting ODCIG resemble the original one as closely as possible. Notice there is no way we can retrieve a result exactly same as the original gather, because the information in azimuth range $(60^{\circ}, 180^{circ})$ is lost in the angle domain CIG. Nonetheless, it is obvious that Figure 5(b) is less distorted than Figure 5(a) is. Our mapping scheme would reduce the artificial noise that arises during the transform of image perturbation from angle back to offset domain.

DISCUSSION

Although it is not a main point in this paper, the computational efficiency is also a crucial challenge for the 3-D extension. As the image gathers become 5-D, the cost of wave-equation operators grows extremely fast as the problem size scales up. Besides choosing a smaller model space, phase-encoded shot records can be used to reduce the number of wave-field simulations. The other bottle neck is the huge amount of disk IO when doing the cross-correlation imaging condition for many subsurface offsets. Based on the recently emerging research topic of compressive sensing, Clapp (2011) proposes a promising idea to reduce the amount of IO required. The author shows that if we *randomly* compute only a subset of the original full 5-D image, for typical seismic data, we can confidently recover the full image without losing useful information.

CONCLUSION

We presented our initial work to extend the proposed RMO-based WEMVA approach to three-dimensional case. We upgraded the theory to deal with multiple azimuth angle-domain CIGs, and we paid close attention to the mapping algorithm between angle and offset domain, in order to reduce artifacts introduced by this irregular mapping. We showed a synthetic example as a verification for our primitive implementation.

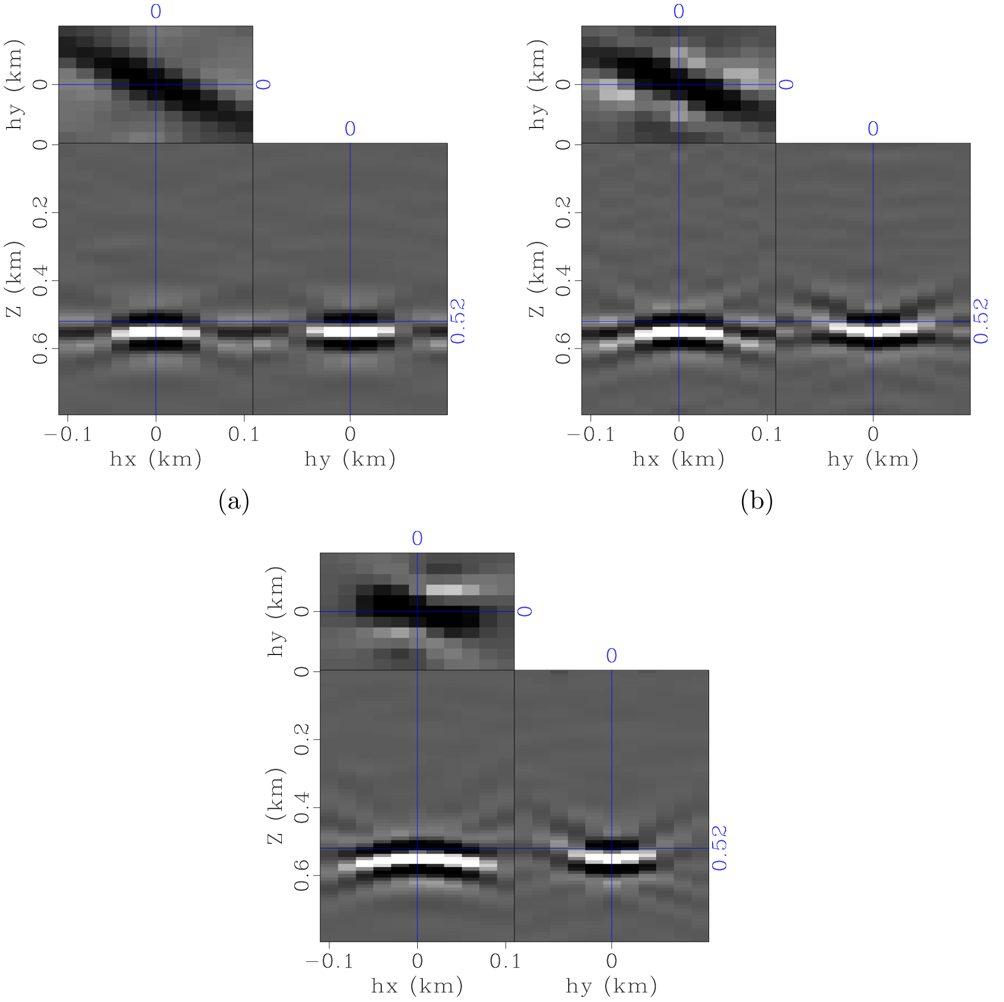

(a)

(b)

(c)

Figure 5: (a) The result of applying forward and backward offset-angle domain transform on an ODCIG, in which the sample-to-sample mapping is used; (b) the same description as (a), except that the patch-to-patch mapping is used. The original ODCIG is shown in (c). All three gathers are chosen at location $x = 0.2\,\text{km}, y = -0.06\,\text{km}$. Notice that the intermediate ADCIG we generate does not have full azimuth coverage ($[60°, 180°]$ excluded), therefore an exactly identical reconstruction of the original ODCIG is not possible. [**CR**]

ACKNOWLEDGEMENT

We thank Yaxun Tang for the one-way wave-equation propagator used in this project.

REFERENCES

Biondi, B., 2003, Amplitude balancing of 3-D angle-domain common-image gathers: SEP-Report, **114**, 45–56.

Biondi, B. and P. Sava, 1999, Wave-equation migration velocity analysis: SEG Technical Program Expanded Abstracts, **18**, 1723–1726.

Biondi, B. and W. W. Symes, 2004, Angle-domain common-image gathers for migration velocity analysis by wavefield-continuation imaging: Geophysics, **69**, 1283–1298.

Biondi, B. and T. Tisserant, 2004, 3D angle-domain common-image gathers for migration velocity analysis: Geophysical Prospecting, **52**, 575–591.

Clapp, R. G., 2011, Imaging using compressive sensing: SEP-Report, **143**, 149–158.

Luo, Y. and G. T. Schuster, 1991, Wave-equation traveltime inversion: Geophysics, **56**, 645–653.

Symes, W., 2008, Migration velocity analysis and waveform inversion: Geophysical Prospecting, **56**, 765–790.

Tang, Y., C. Guerra, and B. Biondi, 2008, Image-space wave-equation tomography in the generalized source domain: SEP-Report, **136**, 1–22.

Tisserant, T. and B. Biondi, 2003, Wavefield-continuation angle-domain common-image gathers in 3-D: SEP-Report, **113**, 211–220.

Zhang, Y. and B. Biondi, 2011, Moveout-based wave-equation migration velocity analysis: SEP-Report, **143**, 43–58.